Applied Surface Science 575 (2022) 151732

Contents lists available at ScienceDirect

Applied Surface Science

journal homepage: www.elsevier.com/locate/apsusc

Full Length Article

Laser-assisted preparation of highly-efficient photocatalytic nanomaterial based on bismuth silicate

A.V. Shabalina [a,*], E.D. Fakhrutdinova [a], A.G. Golubovskaya [a], S.M. Kuzmin [b], S.V. Koscheev [c], S. A. Kulinich [d,e,*], V.A. Svetlichnyi [a], O.V. Vodyankina [a]

[a] Tomsk State University, Tomsk 634050, Russian Federation
[b] G.A. Krestov Institute of Solution Chemistry of the Russian Academy of Sciences, Ivanovo 153045, Russian Federation
[c] Boreskov Institute of Catalysis SB RAS, Novosibirsk 630090, Russian Federation
[d] Tokai University, Research Institute of Science and Technology, Hiratsuka, Kanagawa 259-1292, Japan
[e] Far Eastern Federal University, Vladivostok 690091, Russian Federation

ARTICLE INFO

Keywords:
Bismuth silicate
Laser ablation in liquid phase
Nanoparticles
Laser irradiation of colloids
Photocatalysis

ABSTRACT

Having a wide range of applications, bismuth silicate-based materials (BSO) attract attention of numerous researchers. Typically, they are synthesized either from active chemicals or through high-energy impact on their precursors. The present work is the first report on BSO-based nanomaterials prepared via laser processing in liquid phase in which the following two-step scheme was realized: (1) Individual colloids of Bi- and Si-based nanoparticles were obtained via ablating their metallic targets in distilled water and then mixed; (2) Post-treatment of the mixed colloid was performed with the same laser beam as in stage (1). The products obtained after drying of non-treated and post-treated mixed colloids (denoted as samples BSO and BSO_hν, respectively) were carefully characterized using a set of microscopic, spectroscopic and electrochemical analyses, after which their photocatalytic performance in presence of model organic dye (rhodamine B) and phenol was tested. The additional laser treatment was found to lead to active interaction between Bi- and Si-containing species and stimulated formation of phases with Bi-O-Si bonds. The post-irradiated sample BSO_hν showed improved stability and catalytic performance, thus opening avenues for wider use of laser processing in liquids as a method allowing for preparation of nanostructures with complex chemical composition.

1. Introduction

Bismuth-containing silicates (Bi_2SiO_5, $Bi_{12}SiO_{20}$, and $Bi_4Si_3O_{12}$) are known as quite attractive materials for applications in a number of different fields. For instance, they are used in acoustic and optical devices [1,2], in capacitors (including integrated and thin-film capacitors) [3,4], in nanothermometers [5,6], as well as phosphors [7,8], sensor components [9], and as bioactive materials [10]. Their photo-refractive properties allow for their application as spatial light modulators [11], or even for holographic grafting recording [12]. There are also examples of bismuth silicates (BSOs) used as catalysts for biodiesel production [13], and as material for fuel-cell cathodes [14]. However, the most active area for BSO applications is photocatalysis, where BSO-based materials were tested for water purification [15], including organic dye removal [16], with the most popular object to decompose being rhodamin B (Rd B) [17-21].

BSO and BSO-based materials are prepared in very different forms. So far, with different synthetic methods employed, their glasses [5,22-24], ceramics [4], single crystals [11,12], films and coatings [3,15,18], nanofibers [2,16,25], powders [21,26-28] (including core@shell structures [29]), and porous materials [14,30] were reported. Among the most common methods, electrospinning [2,25], spin-coating [18], molten-salt method [27], chemical synthesis on silica support [29], and post-synthetic modification [30] were mentioned. At the same time, the most popular approaches are still solvothermal and hydrothermal methods [13,21,31] and sol–gel synthesis [4,8,10,17,28], including the Pechini method [19,20].

Generally, to prepare BSO materials, either active precursors [10,17,32] or complex and high-energy treatments [2,27] are used. Nevertheless, new preparative approaches are still anticipated which would use less chemicals and yield high-quality materials in a most controllable, reproducible and cost-efficient way. In light of this, using

* Corresponding authors at: Tokai University, Hiratsuka, Kanagawa 259-1292, Japan (S.A. Kulinich).
E-mail addresses: shabalinaav@gmail.com (A.V. Shabalina), skulinich@tokai-u.jp (S.A. Kulinich).

https://doi.org/10.1016/j.apsusc.2021.151732
Received 22 July 2021; Received in revised form 22 October 2021; Accepted 24 October 2021
Available online 28 October 2021

high-energy laser irradiation to prepare BSO nanomaterials from quite inert Bi- and Si-containing components looks an attractive and feasible approach, if properly realized in practice.

In the present work, we demonstrate that the pulsed laser ablation in liquid (PLAL) method [33,34] can be used to prepare BSO-based nanomaterials from metallic Bi and Si plates. The method consists in irradiation of a solid target immersed into liquid medium with high-power laser beam, which results in generation of nanostructures [33]. Different products for different applications can be obtained by PLAL depending on chosen laser parameters, as well as target and liquid medium. For example, a variety of compounds for catalytic applications were produced by this approach [35,36]. As a versatile technique, PLAL can be performed in several modifications, with different lasers, set-ups (batch, flow, flow jet, etc.), with different target forms (as bulk plate, pressed powder, powder dispersion, colloid, etc.), and using liquid media with different composition [37,38].

Importantly, since very high temperatures and large temperature gradients are achieved locally during PLAL processing, nanomaterials with unique morphology and phase/chemical composition were often reported [33]. Based on this, the main motivation of the present study was to achieve formation of BSO-based nanostructures during laser irradiation of colloid (LIC) stage when Bi- and Si- based colloids prepared via PLAL treatment of their corresponding targets were mixed and then post-processed with the same laser beam.

While metallic Bi nanoparticles (NPs) and bismuth oxide-based NPs obtained via PLAL were previously mentioned [39,40], no reports on BSO nanomaterials obtained by PLAL are available in the literature, except for our previous work devoted to fragmentation of BSO prepared by another method [41]. Therefore, this work is the first report on BSO-based nanomaterials prepared via laser processing which uses a two-step scheme: (1) First, individual colloids of Bi- and Si-based NPs and species were obtained via PLAL of their corresponding targets; (2) Post-treatment of the two mixed colloids was performed with the same beam, leading to the final BSO-based product. All products were carefully characterized, and two samples, i.e. mixed sample formed by Bi- and Si-based colloids and its LIC-treated counterpart, were finally compared in terms of their performance as photocatalysts destroying model organic dye and phenol. As a result, the post-irradiated BSO product showed improved stability and performance.

2. Experimental

2.1. Material preparation procedures

The whole preparation procedure is presented in Fig. 1. First, Bi (99.9%) and Si (99.99%) plates were ablated separately as targets in distilled water by means of a Nd:YAG laser (LS-2131 M, LOTIS TII, Belarus) with 1064 nm wavelength, 7 ns pulse duration, frequency of 20 Hz. The synthesis was carried out in cylindrical glass reactors with a volume of 100 ml. Laser beam was focused on the target surface through the side wall, and Bi and Si targets were ablated in pure water for 7 and 40 min, respectively. For each target, optimum energy density was chosen individually based on its thermophysical characteristics. The power density at the target surface was 150 and 400 MW/cm^2 for Bi and Si targets, respectively, which resulted in dark-brown and cloudy rust-colored colloids. The concentration of generated colloids was evaluated through the weight loss of their corresponding targets to be 600 and 200 mg/l for Bi and Si, respectively. Samples Bi_powder (of grayish-white) and Si_powder (of deep-brown color) were then obtained via drying the initial colloids in air at 60 °C. The experimental protocol used was previously described in greater detail in our previous work [42].

Second, to obtain the ternary material, both freshly prepared Bi and Si colloids were mixed in the atomic ratio Bi:Si equal to 2:1. The mixed colloids were in fresh form, without separation, centrifugation and redispersion in new medium. The actual Bi:Si ratio in samples BSO and BSO_hν (as powders) was controlled using wavelength dispersive X-ray spectroscopy, WDX (an XRF 1800 analyzer from Shimadzu, Japan). For different experiments, it was found to vary from 2.03:0.97 to 1.97:1.03. After mixing the initial individual colloids, two different processing approaches were used. The brownish-black sample BSO is seen in Fig. 1

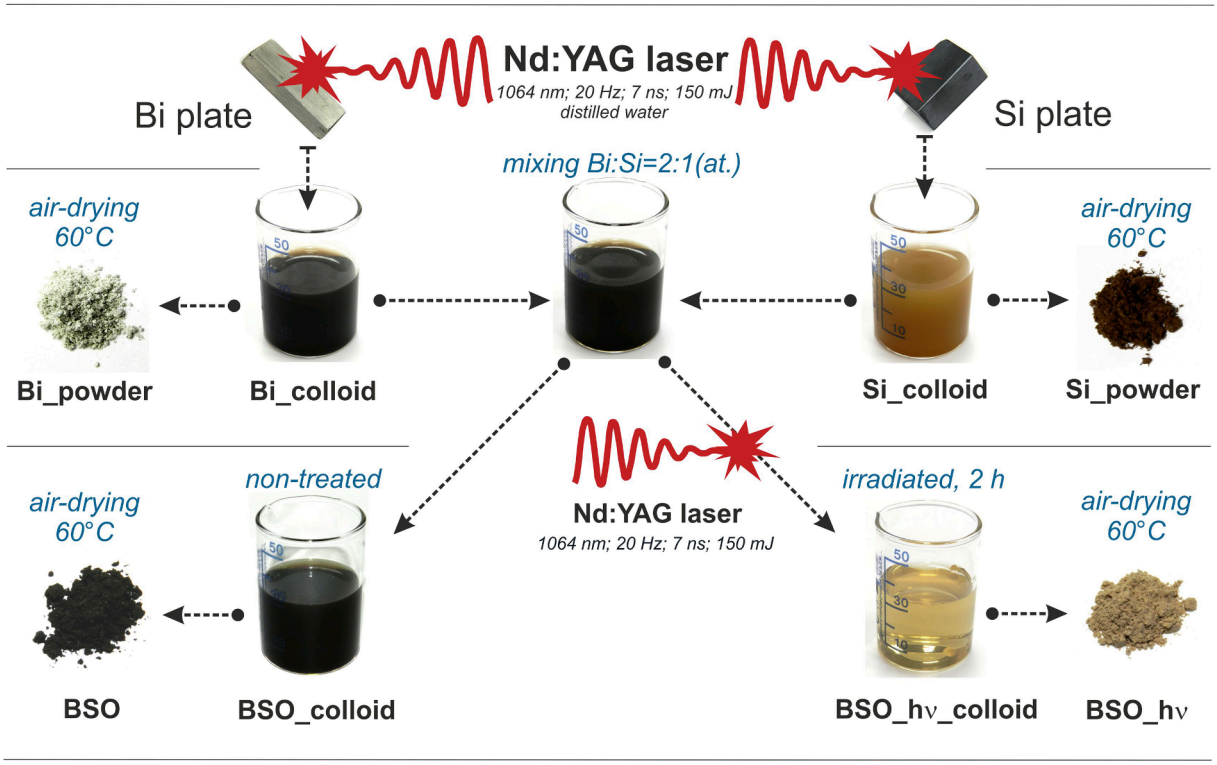

Fig. 1. Schematic presentation of all samples described in this study, their preparation and appearance.

to be prepared via air-drying of the as-prepared mixed colloid (sample BSO_colloid) at 60 °C. At the same time, its laser-processed counterpart, sample BSO_hν_colloid, was produced via irradiating sample BSO_colloid by focused laser beam for 2 h using the same laser parameters as those applied to prepare the initial Bi and Si colloids. This time, during laser processing, the colloid changed its color from dark-brown to pale-yellow and turned completely transparent (see sample BSO_hν_colloid in Fig. 1). Upon air-drying at 60 °C, it gave rise to sand-colored sample BSO_hν.

2.2. Sample characterization

The microstructure of powder samples was studied using transmission electron microscopy (TEM, HT-7700 instrument from Hitachi, Japan) and scanning electron microscopy (SEM, Vega 3H Tescan, Czech Republic). During microscopic studies, at least 10 images for each sample were analyzed, after which the most representative ones were selected to demonstrate all particle morphologies. Particle size distribution for the fine fraction of the materials was calculated from TEM images by measuring diameters of at least 2000 particles for each sample.

Specific surface area was determined via low-temperature adsorption/desorption of N_2 according to the BET method using a TriStar II 3020 tool (Micromeritics, USA). Prior to the adsorption stage, the samples were degassed in vacuum (10^{-2} Torr) at 200 °C for 2 h. X-ray diffraction (XRD) patterns were registered using an XRD 6000 diffractometer (Shimadzu, Japan) with CuKα irradiation, after which phase analysis was performed using the PDF-4 database. X-ray photoelectron spectroscopy (XPS) data were obtained using an ES-300 spectrometer (Kratos Analytical Ltd., UK) with MgKα as irradiation source. Taking into account sample charging, all binding energies were corrected by referencing to the adventitious C 1 s peak at 285.0 eV.

FTIR and Raman spectra were obtained using a Nicolet 6700 spectrometer (Thermo Fisher Scientific, USA) and an inVia Raman microscope (Renishaw, UK), respectively. Diffuse-reflectance UV–Vis absorption spectra (DRS) were collected using a Cary 100SCAN spectrophotometer (Varian, Australia) with a DRA-CA-30I accessory (Labsphere, USA). Band gap value was then calculated using the Tauc method.

Zeta potential of colloids was measured on an Omni S/N (Brookhaven, USA) in ZetaPALS mode and with the help of a BI-ZTU autotitration module (Brookhaven, USA) used for pH adjustment. The pH of colloids with the concentration of 0.5 mg/ml was controlled using diluted aqueous HNO_3 and KOH.

The flat band potential (E_{fb}) and donor density for analyzed nanomaterials were obtained from their Mott-Shottky (M−S) plots. The latter plots were registered using an electrochemical workstation CH 660D (CH Instruments, USA) with a three-electrode cell. Samples were dispersed in polystyrene solution in dichloroethane and placed on glassy carbon working electrodes. A Pt plate and Ag/AgCl with 1 M KCl were used as a counter electrode and a reference electrode, respectively. The frequency of 1 kHz was fixed and potential was swept from 0 to –0.6 V to collect data necessary for M−S plots.

To calculate the mobility of charge carriers in samples, the Mott-Gurney law was used. For this, a solid electrochemical cell consisting of two contact electrodes (d = 5 mm) and compressed powder tablet between them (thickness of 1 mm) was utilized. Linear sweep voltammograms in the range from 0 to + 10 V, and electrochemical impedance spectra were registered on an SP300 potentiostat (BioLogi, France) to determine the dielectric constants of materials. The obtained data were then treated using the ZView (Scribner, USA) and EC-Lab (BioLogic, France) software.

Photocatalytic activity was studied through decomposition of aqueous solutions of rhodamine B (Rd B) and phenol (Ph) as model compounds under illumination from an LED source (375 nm, half-width at half-maximum of 10 nm). The initial concentrations were 5×10^{-6} and 5×10^{-5} M for Rd B and Ph, respectively. A sample of titania P 25 (Merck) was also used as a reference for comparison. Prior to photocatalytic tests, dispersions of tested nanomaterials (15 mg per 30 ml) in aqueous Rd B (or Ph) were subjected to so-called “dark” stage which lasted for 1 h and provided proper sorption of model pollutant on the catalyst’s surface. The concentration of organics over time was determined using a Cary 100SCAN spectrophotometer (Varian, Australia).

3. Results and discussion

3.1. Results of TEM, XRD and XPS studies

The main stages where the samples were characterized are presented in Fig. 1. During preparation and other manipulations, we investigated the following materials:

- Sample Si_powder, which was a dry powder prepared from Si colloid (the latter colloid was thoroughly described in our previous reports [43,44]);
- Sample Bi_powder, which was a dry powder prepared from Bi colloid (also previously described elsewhere [45]);
- NPs taken from as-prepared sample Bi_colloid not subjected to a long-term drying (their analysis allowed us to reveal the state of Bi NPs in the freshly prepared colloid);
- Dry powder obtained after mixing Bi and Si colloids (non-irradiated with laser, sample BSO);
- Dry powder obtained after laser-irradiation of mixed Bi and Si colloids (sample BSO_hν).

3.1.1. Components before mixing

Sample Bi_powder, i.e. material produced via PLAL of Bi in water and then dried in air, was previously characterized in work [45]. It was reported to consist of crystalline plates of 500 nm on average and had its specific surface area of 1.3 m^2/g (based on BET measurements). The growth of such plates is well consistent with previous results reported elsewhere [46]. It was revealed from the XRD data that such plates contained monoclinic α-Bi_2O_3, tetragonal bismuth subcarbonate, and orthorhombic bismuth subcarbonate hydroxide as components [45]. Since bismuth is well-known for its high affinity to carbon, it was assumed that the carbonate phases were formed during colloid’s drying in air. The question still remained whether bismuth oxide presented in the colloid was formed during laser treatment of Bi target or it was generated during drying process. Previously, Bulmahn *et al.* [46] showed that oxide nanoplates grew after drying or keeping their ablated colloid for some time in air. To reveal this in the present work, and to minimize contact time with air, the freshly prepared sample Bi_colloid was immediately drop-cast on a microscopic copper grid, air-dried for a short period of time and then placed into microscope’s vacuum chamber. Thus prepared sample demonstrated that in its laser-prepared colloid, Bi was in its metallic form, exhibiting spherical NPs of 3 to 35 nm in size, the majority of which being around 10 nm (see Fig. S1, as well as SAED data as inset therein, *Supplementary Materials*). Hence, freshly-ablated colloid of bismuth was in its metallic form before it was mixed with sample Si_colloid.

Samples Si_colloid and Si_powder were also characterized and described in our previous work [43]. Silicon ablated in water was shown to be a colloid of Si NPs with sizes in the range of 2–40 nm, also having SiO_2 and Si@SiO_2 core–shell structures, as well as shapeless elongated species (hereafter referred to as soluble silicon compounds). Upon air-drying, Si@SiO_2 NPs of the same size were formed (with their S_{BET} being of 400 m^2/g) that agglomerated after heating. Thus, before mixing with sample Bi_colloid, sample Si_colloid was a mixture of partly oxidized silicon nanostructures and soluble silicon compounds. Consequently, when freshly prepared samples Bi_colloid and Si_colloid are mixed, they contain metallic Bi NPs (3–35 nm in size), those of Si, SiO_2

and Si@SiO_2, and soluble silicon compounds. Upon mixing, all these components were the only reactants to give rise to new products.

3.1.2. Products of colloid mixing

At first, samples Bi_colloid and Si_colloid were mixed at atomic ratio Bi:Si = 2:1, which gave us sample BSO_colloid. A part of this sample was dried, turning to a brownish-black powder. TEM images of the latter powder (sample BSO) showed agglomerates of nearly spherical NPs of 2.5 to 60 nm in size, with the majority being around 10 nm (Fig. S2a). TEM analysis of the finest fraction does not present the whole picture in case of many nanomaterials, which is why TEM is normally used in combination with SEM. SEM images of sample BSO did not permit easily to distinguish individual large NPs and dense agglomerates of smaller ones. Nevertheless, the fraction of small particles was found to be unquestionably more abundant than that of large ones (in terms of their numbers). The sample is seen in Fig. S2a to demonstrate a slightly asymmetric size distribution peak for its fine fraction, which is well consistent with previously reported data for other laser-generated or laser-processed materials [37,47,48]. The BET specific surface area of this material (characterizing its overall micro-dimensions) was found to be around 41 cm^3/g. The SAED data (inset in Fig. 2a) suggested mainly amorphous nature of the particles obtained. Based on its XRD pattern (Fig. 3), only metallic Bi was found in sample BSO (PDF-4 #04–007-9968), while no diffraction patters of Si-containing compounds were found. The presence of metallic bismuth was also confirmed by SEM images obtained in the back-scattering mode or BSE (*z*-contrast mode). That is, heavier elements (with larger *z*) reflect more electrons, which makes their location look as brighter spots in SEM images. As a result, for example, in a mixture of metal oxide and metallic NPs of the same metal, the latter metallic particles will look brighter than those of metal oxide.

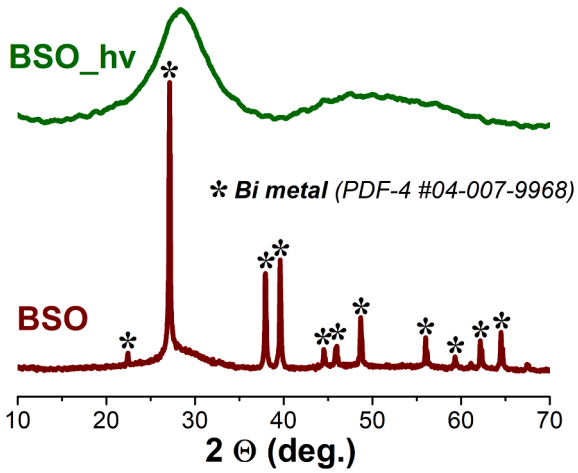

Fig. 3. XRD patterns of samples BSO (brown) and BSO_hυ (green).

In Fig. 2c, metallic Bi NPs are seen as brighter spots surrounded by darker amorphous Si-based background. Thus, one can conclude that sample BSO demonstrates no clear signs of chemical reactions between Bi and Si–containing nanomaterials.

Here, it should be noted that (i) unlike dry sample Bi_colloid, no bismuth oxidation was observed in dried sample BSO; (ii) the structure of dry sample BSO as powder was also found to be different from sample Bi_powder. More specifically, no plate formation but mainly spherical NPs were detected in the mixture of Si and Bi colloids which was not subjected to further irradiation. Presumably, this could be caused by smaller Si NPs (with large surface area) covering bigger Bi NPs, which

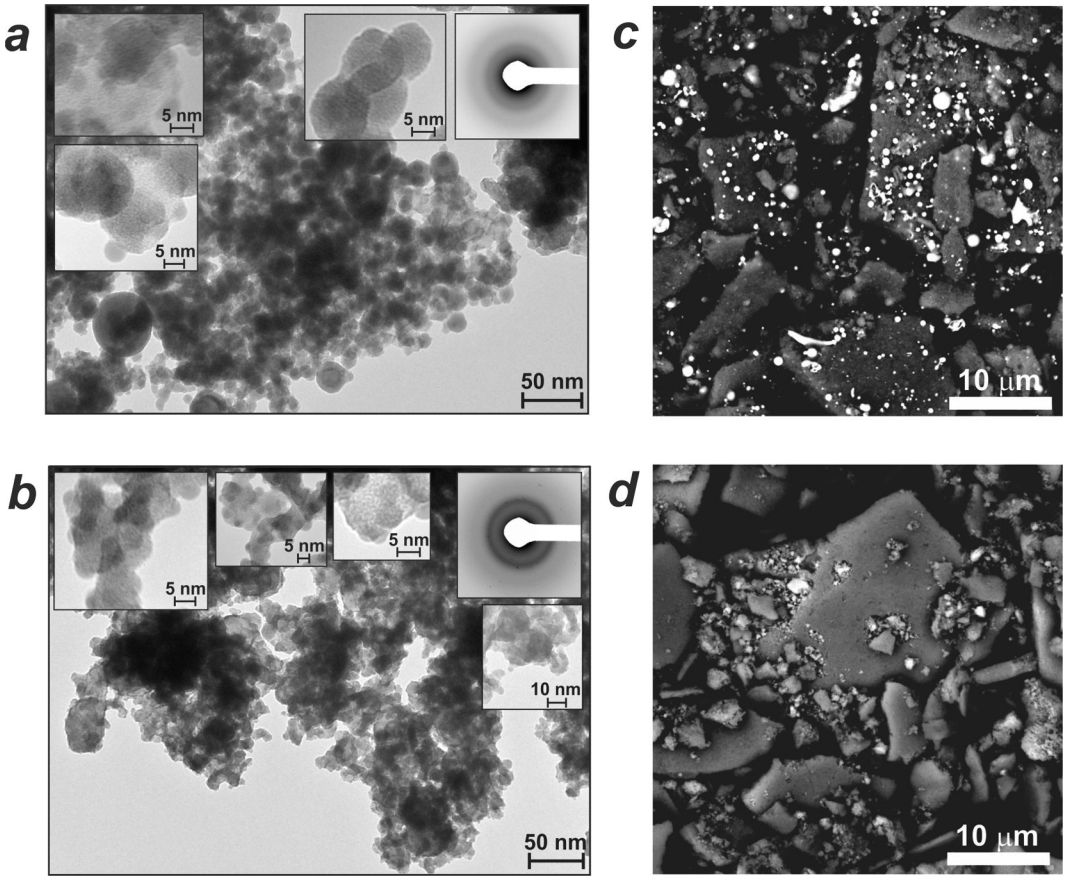

Fig. 2. (a,b) TEM and (c,d) SEM BSE images of samples BSO (a, c) and BSO_hν (b, d). Insets in panels (a) and (b) show SAEDs and TEM images with higher magnification.

thus prevented the latter NPs from oxidation and carbonate-phase formation upon their drying. Also, since the Bi NPs had their surface covered and thus "passivated", they could not recrystallize into plates.

To get more insight about chemical composition, XPS analysis of sample BSO was carried out, with its survey spectrum and elemental composition of its surface presented in Fig.S3 and Table S1, respectively (see *Supplementary Materials*). Fig. 4a, 4c and 4e show narrow-scan XPS spectra of Bi, O, and Si for this sample. The values of binding energy from different sources for the experimental spectra analysis provided in Table S2.

The main component of the Bi 4f spectrum in Fig. 4a cannot be easily related to bismuth oxide (Table S2). According to report [17], the shift of this doublet observed in our work clearly points at the presence of Si-O-Bi bonding on the material's surface. The shoulders observed at lower energy (157 eV and its companion at 162.3 eV) are indicators of metallic Bi [49]. Since XPS is a method analyzing a very shallow surface layer, the conclusion on the content of metallic Bi cannot be drawn from XPS alone. As discussed above, upon mixing two colloids, Bi based particles from sample Bi_colloid were covered with smaller NPs and other components of sample Si_colloid. Thus, the content of metallic Bi in the surface layer of the mixed sample BSO is not high.

The Si 2p spectrum of sample BSO was deconvoluted using four components (Fig. 4c). Accordingly, the sample was concluded to have the following surface species (Table S2, also see articles [49,50]): carbides (101.0 eV), silicates (102.1 eV), SiO_2 or silicates (103.2 eV) and SiO_2 (104.1 eV). XPS spectra of Si NPs previously prepared with the same setup and corresponding to sample Si_powder (prepared from Si_colloid before it was mixed with Bi NPs) can be found in our previous report [44]. Since only signals of Si and SiO_2 bonds were observed for such Si NPs [44], obviously mixing samples Si_colloid and Bi_colloid led to some interactions between their components.

In the O 1 s spectrum of sample Si_powder, mainly SiO_2 bonds were previously observed [44]. After mixing Si and Bi- based colloids, the O 1 s spectrum of sample BSO was curve-fitted with two components (Fig. 4c) which were assigned to oxygen from lattice O (from silicates or Bi_2O_3) observed at 530.2 eV and to SiO_2, silicates or carbonates seen at 532.4 eV (Table S2, [51]). This also points at interactions between Si and Bi components in the mixed colloid even without additional laser treatment.

The XPS C 1 s spectrum recorded for sample BSO is shown in Fig. S4. It demonstrates carbides, carbonates, amorphous C, and possibly groups such as –COOH and –CO as surface species. As mentioned above, the Si 2p spectrum of this sample also showed carbide species; hence the sample contains some amount of surface SiC bonds.

Thus, on the basis of the above described results, one can conclude that sample BSO had metallic Bi as its main component, which was covered with layers of SiO_2 and amorphous SiO_x, and some amount of SiC. Certain degree of chemical interaction between Bi and Si could be observed, with some amount of surface Si-O-Bi bonds detected by XPS. The latter bonds could be product of fast reactions between Bi NPs when those came to contact with soluble silicon compounds, which occurred shortly after mixing freshly-prepared colloids of Bi and Si. Importantly, however, such Si-O-Bi species were present at trace amounts.

3.1.3. *Products of mixing and subsequent LIC processing*

As shown in Fig. 1, the mixture of samples Bi_colloid and Si_colloid was subjected to LIC processing. When choosing the irradiation time, we checked both absorption spectra and visual color changes of the irradiated sample. After irradiation for as long as 2 h, the sample changed color from dark-brown to pale-yellow and turned transparent (see Fig. 1), showing no further spectral changes. After drying this colloid, a sand-colored powder of sample BSO_hν was obtained. Its TEM image is seen in Fig. 2b to demonstrate agglomerates of rather shapeless and amorphous particles with typical sizes between 3 and 50 nm. The size distribution for its fine fraction obtained from TEM images is presented in Fig. S2b. It is seen to be slightly narrower than that of sample BSO (Fig. S2a), which is believed to be explained by secondary interaction of its particles with laser beam, as well as partial fragmentation of larger particles under irradiation.

The specific surface area of about 55 cm^3/g was measured for sample BSO_hν, being larger than that of its non-treated BSO counterpart. The SEM BSE image of sample BSO_hν is presented in Fig. 2d. It is seen that the number of bright spots present in the irradiated sample BSO_hν is much smaller than in sample BSO (Fig. 2c), while in general the gray color of its "matrix" is more homogeneous. This implies that during irradiation with laser beam, metallic Bi inclusions reacted with other components of the system, forming much more homogeneous material in terms of phases.

The XRD pattern of sample BSO_hν showed its mainly amorphous nature, as well seen in Fig. 3 (green pattern). However, some reflexes could be seen in its SAED pattern (inset in Fig. 2b) which can be attributed to SiO_2 (PDF-4 #00–012-0708), $BiO_{1,5}$ (PDF-4 #04–005-

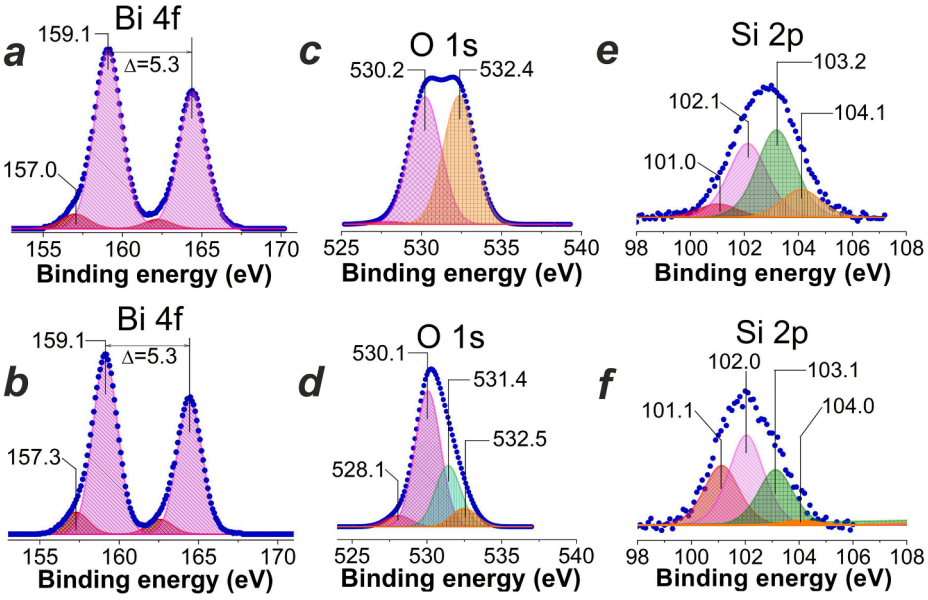

Fig. 4. Narrow-scan XPS spectra of samples BSO (a,c,e) and BSO_hν (b,d,f). Peaks of Bi 4f (a,b), O 1 s (c,d) and Si 2p (e,f) are given along with results of their curve-fitting.

4788) and $Bi_2Si_3O_9$ (PDF-4 #04–013-6743) phases. This observation can point at possible formation of a joint phase that contains both Bi and Si atoms. However, the forming phases could be amorphous and as such generally invisible for XRD analysis. This can also be confirmed by the fact that thermal treatment of the sample at 600 °C led to the complete formation of the Bi_2SiO_5 phase (PDF-4 #00–036-0287, see Fig. S5).

Analysis of XPS spectra of BSO_hν exhibited in Fig. 4b, 4d, 4f permits to conclude that the Bi/O and Bi/Si ratios increased in comparison with sample BSO (Table S1). This finding also permits to conclude that sample BSO had more O and Si on its surface, thus also implying that in sample BSO_hν the components were mixed more homogeneously, presumably down to atomic level. In other words, some chemical interactions took place during laser treatment.

The Bi 4f core-level spectrum of sample BSO_hν is generally identical to that of its BSO counterpart, implying Si-O-Bi and some metallic Bi species on both surfaces (see Fig. 4a and b, Table S2). Since metallic bismuth is not well-seen in the SEM image of the laser-irradiated sample (Fig. 2d), its amount is believed to be very low. Therefore, it can be assumed that only the largest metallic Bi NPs could survive the second laser treatment, while the majority of metallic Bi reacted under irradiation (see also SEM images and discussion above).

In Fig. 4f, all the four components of the XPS Si 2p spectrum of sample BSO_hν can be assigned to SiO_2 and silicates (Table S2). As seen in Fig. 4e, a part of Si atoms in sample BSO were present in the form of carbide SiC (see Table S2 and discussion above). At the same time, in the spectrum of sample BSO_hν (Fig. 4f) the signal at 101.1 eV is more likely to belong to other species rather than SiC (Table S2). In parallel, the XPS C 1 s spectrum of the laser-irradiated sample showed a decrease in surface carbides and increase in surface carbonates and functional groups (see Fig. S4b and Table S2). Therefore, it is reasonable to conclude that surface SiC phase observed for non-irradiated sample BSO interacted with other components and disappeared during laser irradiation.

The O 1 s spectrum of sample BSO_hν demonstrated the biggest contrast when compared with that of sample BSO (Fig. 4c and 4d). This implies that the nature of oxygen states changed significantly after additional laser processing of mixed Bi and Si colloids. A component at 532.5 eV almost disappeared, while two additional components emerged at 528.1 and 531.4 eV. The components of the XPS O 1 s peak are spread wider in Fig. 4d, which may point at the presence of Si-O-Bi species (Table S2), while the new component emerging at 531.4 eV belongs to silicates, carbonates or hydrates (see Table S2 and [51-53]). So, the significant changes found in surface oxygen species once again point at chemical interactions between Bi- and Si-based species during LIC treatment.

It is thus clear that sample BSO_hν has more products of chemical reactions between Bi and Si colloids. Possibly, when stimulated by laser irradiation, Bi further reacts with soluble silicon compounds. It could also react with Si, SiO_2 and Si@SiO_2 nanostructures as main components of the Si colloid. In any case, additional irradiation of the mixture of samples Bi_colloid and Si_colloid led to a product with new composition and structure, and most importantly with Bi-Si-O species as its main component.

Thus, when a mixture of Si and Bi colloids is exposed to high-power focused pulsed laser irradiation, this initiates interactions between Bi and Si NPs and leads to the formation of more complex phases, i.e., bismuth silicates. In this work, we did not aim at studying thoroughly all the mechanisms involved in the formation of these new phases under LIC treatment, which will be a goal of our future research.

3.2. Spectroscopic study

Absorption FTIR spectra of samples BSO and BSO_hν are presented in Fig. 5a. The set of absorption bands seen in the range from 400 to 600 cm^{-1} is quite difficult to interpret. According to the literature [54-56], they can be assigned to different vibrations related to Si-O and Bi-O bonds, both in bismuth oxides and silicates. For sample BSO_hν subjected to high-power laser irradiation, a pronounced peak appears around 890 cm^{-1}, which can be attributed to the vibrations of $HSi\text{-}O_3$. This correlates with the data previously reported elsewhere [57,58], including those obtained for silicon laser-ablation in water [44,58]. Also, for this sample, a shoulder around 845 cm^{-1} can be distinguished, which is attributed to the vibrations of Bi-O-Si [55–57,59]. The absorption band observed in the range of 1000–1200 cm^{-1} belongs to longitudinal-optic (LO) and transverse-optic (TO) components of the stretching vibration mode in Si-O-Si bonds found in $(SiO_4)^{-4}$ and $(SiO_6)^{-6}$ rings [44,54]. For the sample obtained from BSO_colloid subjected to laser post-treatment, there is a pronounced maximum at 1100 cm^{-1}, which is attributed to the stretching Si-O-Si mode in amorphous SiO_2. For the non-irradiated sample BSO, the maximum associated with Si-O-Si vibrations is shifted to 1040 cm^{-1}. Absorption in the range of 1300–1500 cm^{-1} seen for both samples is most likely related to carbonaceous components (stretching modes of CO_3^{-2} or other carbon-containing species) whose presence was detected by XPS (see section 3.1). A small peak at 1640 cm^{-1} and bands in the range of 2500–3900 cm^{-1} (not shown in Fig. 5) correspond to the bending and stretching vibrations of H_2O and OH-groups [54], which is not surprising since the samples were generated in water and were not subjected to heat treatment above 50–60 °C.

Thus, the FTIR spectra in Fig. 5a permit to assume that additional laser processing: (i) increased the proportion of $HSi\text{-}O_3$ bonds; (ii) led to redistribution of $(SiO_4)^{-4}$ and $(SiO_6)^{-6}$ rings; (iii) stimulated formation of

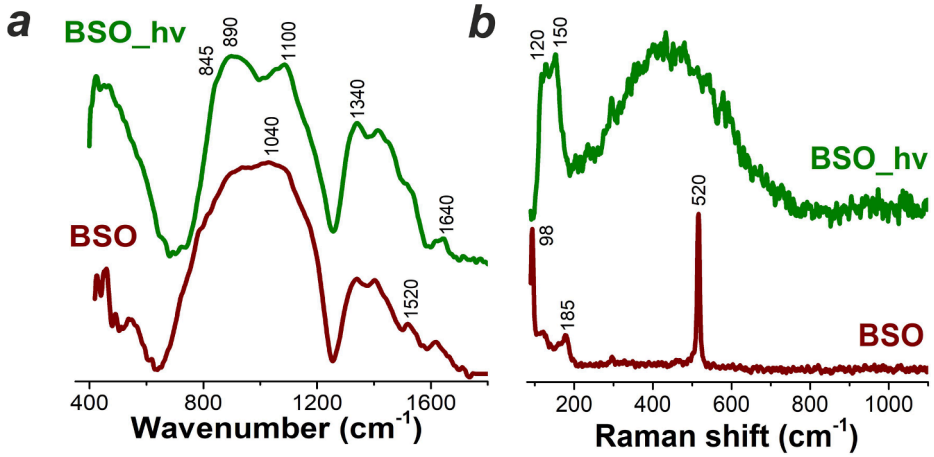

Fig. 5. (a) FTIR absorption and (b) Raman shift spectra of samples BSO (brown) and BSO_hν (green).

the Bi-O-Si interface.

Raman shift spectra are seen in Fig. 5b to be fundamentally different for these two samples. The spectrum of sample BSO clearly shows a peak of crystalline silicon at ~ 520 cm^{-1} [60], agreeing well with previous results of others who also detected crystalline silicon in laser-produced and then dried colloids [43,44]. It is thus seen that this sample had non-reacted silicon coming from the original dispersion, which was not detected by XRD and SAED. The two bands at ~ 98 and 185 cm^{-1} refer to vibrations of metallic bismuth, which was previously confirmed by XRD data. A typical Raman spectrum of bismuth is known to have two modes at ~ 71 and 98 cm^{-1} which are coming from first-order optical vibrations in rhombohedral bismuth and correspond to doubly degenerate E_g and nondegenerate A_{1g} phonon modes, respectively [61,62]. There is also a weak broadened band of second-order vibrations of metallic bismuth at 185 cm^{-1} consisting of three overtones of close frequencies [62,63].

As was mentioned in section 3.1, drying the colloid of individual bismuth NPs in air was found to result in their complete oxidation. However, in a mixture with its silicon colloid counterpart, such oxidation did not occur. Silicon, its oxides and soluble silicon compounds from its colloid were believed to cover bismuth NPs, protecting them from oxidation and restructuring. In addition, small amounts of product formed upon mixing bismuth and silicon colloids (previously described in section 3.1) could also act as protective layer and prevent fast oxidation into bismuth oxides. Thus, the main structures found in the Raman spectrum of sample BSO were crystalline non-reacted silicon and metallic bismuth.

The Raman spectrum of laser-treated sample BSO_hν had a very low intensity and exhibited two bands in the short-wavenumber range and a wide structureless band around 200–600 cm^{-1} with an apex at ~ 400 cm^{-1}, which is characteristic of an amorphous material. Based on band position, one can assume that they all reflect initial formation stage of β-bismuth oxide and/or bismuth silicate Bi_2SiO_5. The main signals are seen in the range of 120–150 cm^{-1} and refer to heavy metal ion vibrations, i.e. those involving the motion of Bi^{+3} cations in BiO_3 pyramidal units from bismuth oxide [64,65], as well as to lattice vibrations in bismuth silicate [64,66]. The broad band with a maximum at about 400 cm^{-1}, as first assumption, can be associated with the most intense vibrations at 295 and 372 cm^{-1} characteristic of Bi_2SiO_5 [66], which is believed to be forming in this sample.

Thus, FTIR and Raman data confirmed that additional LIC treatment of the mixed Si and Bi colloid stimulated formation of nanomaterials that contain both Bi and Si atoms in one phase (bismuth silicates), while metallic Bi and non-reacted Si species remained mainly unreacted in the similar sample BSO which was not subjected to LIC processing.

3.3. Optical properties

The optical properties of two obtained powders were investigated by means of the UV–vis diffuse reflectance technique (Fig. 6a). Sample BSO, being a black powder, exhibited structureless absorption within a wide range of spectrum (see brown spectrum in panel (a)). This can be related to presence of metallic bismuth as was detected by XRD and Raman shift spectroscopy. Its laser-irradiated counterpart (sample BSO_hν) showed quite different optical properties (green spectrum in panel (a)). Irradiation-caused structural transformations are well-seen to lead to appearance of spectral features in sample BSO_colloid that are characteristic of semiconducting oxides and bismuth silicates. Unlike the featureless absorption demonstrated by the non-irradiated sample, a pronounced absorption edge up to ~ 360 nm and a wide shoulder between 400 and 600 nm are seen in the spectrum of the treated sample.

An intense absorption observed in the UV range can be attributed to metasilicate Bi_2SiO_5 as it begins forming in the sample. The latter metasilicate is known to be a direct-gap semiconductor with a band gap of about 3.5 eV [54,56]. The same value of E_g was obtained for sample BSO_hν using the Tauc method (Fig. 6b) and the following equation:

$$\alpha h\nu = k(h\nu - E_g)^{\frac{n}{2}}$$

Where $n = 4$ was chosen as a value characteristic of direct-gap semiconductors. The shoulder found in the visible spectral range can be attributed to the diffusion of the absorption band edge (the so-called Urbach tail), which is typical for small-sized defects and disorders in semiconductor nanostructures and thin films [67-69]. Alternatively, this could be caused by initial formation of some amount of oxide β-Bi_2O_3 with its E_g of ~ 2.4 eV, which is a non-direct-gap semiconductor that absorbs in this spectral region [54].

3.4. Surface properties

3.4.1. Zeta potential measurements

The dependence of zeta potential of samples BSO and BSO_hν (whose powders were dispersed in water) on pH is presented in Fig. 7. The initial dispersion of powder BSO was found to have pH ~ 7 and the zeta potential of its particles was vastly negative (–33.0 mV). When the pH of its dispersion decreased, the potential gradually went towards positive values, reaching ~ 32.0 mV in acidic medium with pH 3.7 (Fig. 7a). The surface recharging was found to take place at pH of about 5.5.

Its freshly prepared counterpart, sample BSO_hν, is seen in Fig. 7b to demonstrate pH of around 5.5, its zeta potential value being positive and quite high (+25.9 mV). When the acidity of its aqueous dispersion was decreased, the potential decreased, demonstrating that its particles' surface recharged at pH of 7.6. It is worth noting that in alkaline media with pH over 9, the potential of sample BSO_hν increased (Fig. 7b), which is believed to be associated with changes of surface composition occurring in alkali media.

Thus, both powders are characterized with high zeta potential values, which means their dispersions in water should exhibit high stability. This is quite an important characteristic for their potential

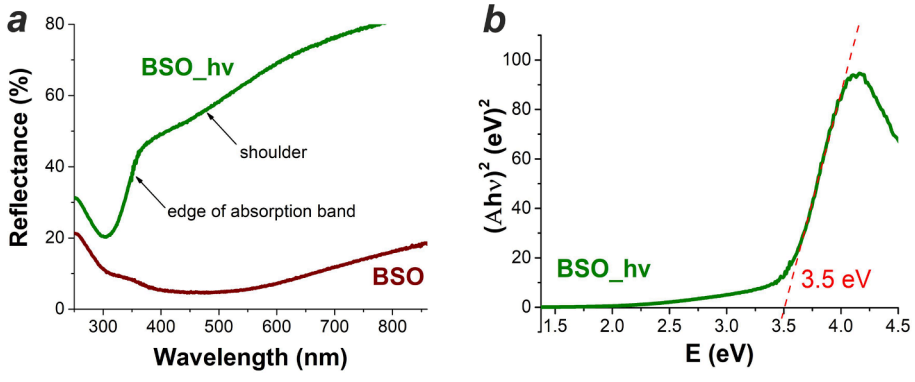

Fig. 6. (a) UV–Vis DRS of samples BSO and BSO_hν as powders. (b) Tauc plots $(Ahv)^2$ vs. photon energy (hv) for sample BSO_hν.

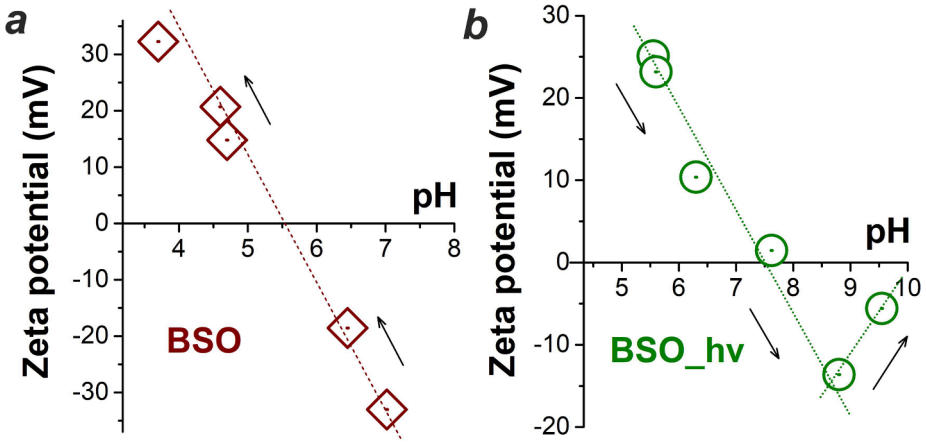

Fig. 7. Zeta potential dependence on pH measured for samples BSO (a) and BSO_hν (b) dispersed in water. Direction of pH change during titration is shown with arrows.

applications, for example, in catalysis or photocatalysis in aqueous media. Interestingly, the sign of the initial zeta potentials of the two samples was different. The colloid prepared via redispersion of sample Bi_powder was not stable (large layered lamellar structures), which is why its zeta-potential was not evaluated. The zeta potential of sample Si_powder was found to be –30.0 mV, which is close to the value registered for sample BSO This allows us to conclude that the surface properties of NPs in sample BSO are determined by those of their precursor particles ablated from Si target in water. This proves one more time that the NPs in sample BSO obtained by mixing consisted of Bi particles from sample Bi_colloid covered with species from sample Si_colloid. Such a coating protected sample BSO from further oxidation, and, as seen in Fig. 7, it also provided its NPs with better stability over pH in comparison with that of sample BSO_hν. The latter sample exhibited a knee-point, implying significant surface composition changes at pH around 9 and larger.

Overall, the zeta potential measurements also confirm that additional irradiation of the joint colloid led to significant changes in both chemical composition of the product material and its surface properties.

3.4.2. *Electrochemical characterization*

To estimate the values of flat band potential (E_{fb}) and the donor density (N_D) in the two materials, the Mott-Schottky (M−S) approach was applied. Note that the non-irradiated sample BSO containing metallic Bi is still covered with silica-based species, which should determine the surface properties of this nanomaterial (see section 3.4.1).

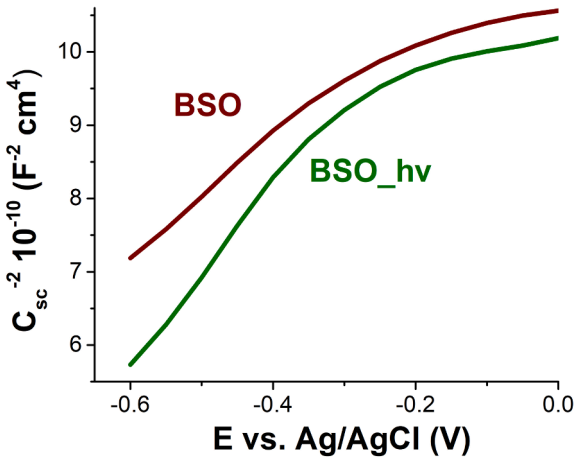

Fig. 8. Mott-Schottky plots for samples BSO (brown curve) and BSO_hν (green curve) obtained in 0.5 M Na_2SO_4 at 1 kHz.

That is why it can be tested as a semiconductor. Fig. 8 demonstrates M−S plots of samples BSO and BSO_hv which are typical of *n*-type semiconductors, while the calculated values of E_{fb} and N_D are given in Table 1. Even though it is known that for *n*-type semiconductors there is often a negative shift in E_{fb} values [70], the obtained data can be analyzed, and at least the calculated values can be compared with each other.

It is seen in Table 1 that calculations for both materials revealed quite similar and rather large donor densities for the samples. Both samples exhibited high negative values of E_{fb}, which might cause their good performance as photocatalysts, for example, for hydrogen production through water splitting. At the same time, sample BSO_hν is seen to be characterized with a lower flat band potential value.

Charge carrier mobility (μ) was estimated using the Mott-Gurney low [71,72] on the basis of the results of linear sweep voltammetry and electrochemical impedance spectroscopy obtained for the powder samples in a solid electrochemical cell. The μ values of about 50 and 3000 $cm^2/V \cdot s$ were obtained for samples BSO and BSO_hν, respectively. Hence, the post-irradiated sample consisting of Bi-Si-O phases exhibited a much better charge carrier mobility, pointing at its better potential for photocatalytic applications.

3.5. *Catalytic activity in photodegradation of organics*

Photocatalytic activity of the materials was evaluated in the decomposition of rhodamine B (Rd B) and phenol (Ph) as model organics in presence of LED irradiation. Spectra of Rd B subjected to photodecomposition are seen in Fig. 9a to demonstrate a hypsochromic shift of the dye's absorption maximum in presence of both materials (for brevity, only spectra for sample BSO_hν are presented). Such a hypsochromic shift is known to be associated with formation of a number of N-diethylated Rd B intermediates (n,n-diethyl-n'-ethylrhodamine, n,n-diethyl- rhodamine, and rhodamine) [73,74]. In Fig. 9a the shift from 553 to 495 nm is seen to proceed stepwise during 4 h of irradiation. The latter peak (at 495 nm) can be attributed to the absorption of rhodamine (Rd), more specifically, Rd 110, which is the product of complete N-diethylation of Rd B [74]. The decrease in intensity at 553 nm can be connected with both N-diethylation of Rd B and Rd B structure

Table 1
Flat band potential and donor density values calculated from the M−S plots for samples BSO and BSO_hν.

Sample	E_{fb} vs. NHE (V)	N_D (m^{-3})
BSO	–1.15	10^{24}
BSO_hv	–0.81	10^{24}

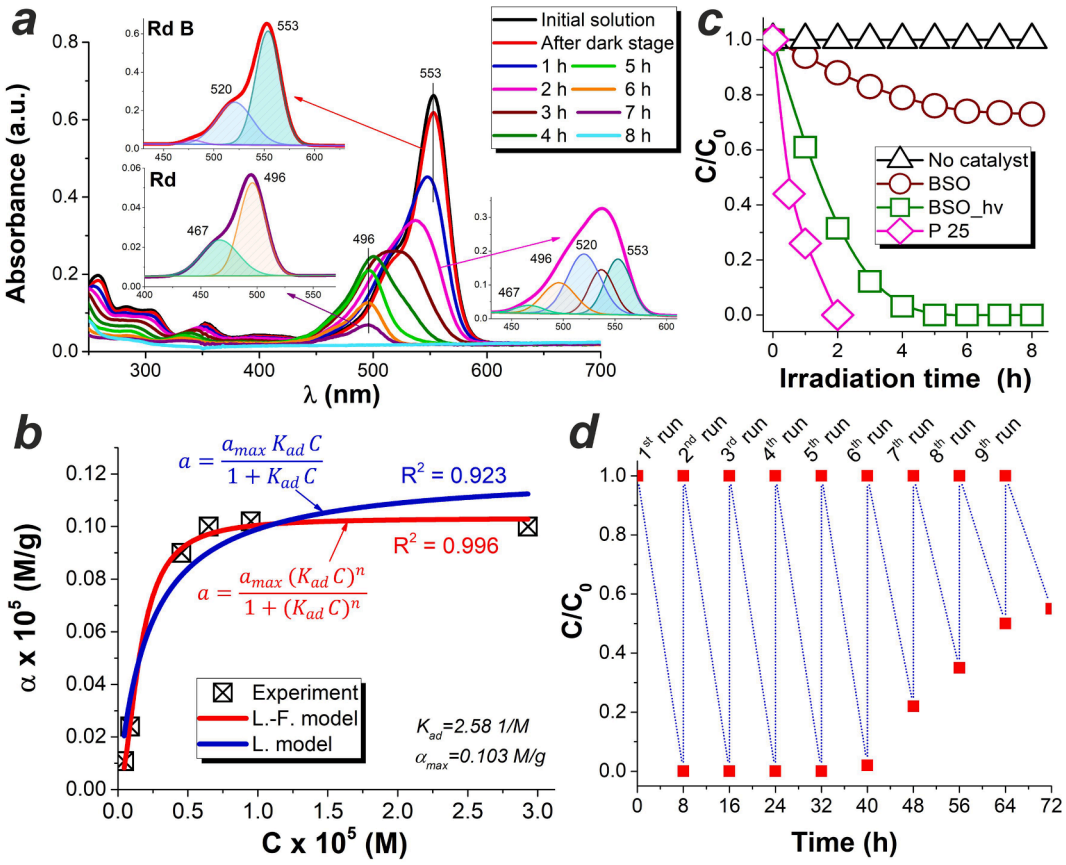

Fig. 9. (a) Temporal changes of Rd B absorption spectrum in presence of BSO_hν. (b) Adsorption isotherm of Rd B on BSO_hν (experimental data, and Langmuir (L) and Langmuir-Freundlich (L-F) models). (c) Kinetic data of Rd B decomposition in presence of samples BSO (brown circles), BSO_hν (green squares), P 25 (pink diamonds) and reference without catalyst (black triangles). (d) Recycling properties of BSO_hν for photocatalytic degradation of Rd B.

decomposition to simpler molecules with lower molecular weight. For sample BSO_hν presented in Fig. 9a, irradiation for 4 h led to complete disappearance of Rd B. At this point, the solution contained N-diethylation intermediates, and further irradiation resulted in cleavage of their aromatic rings followed by gradual mineralization. Continuous irradiation for 8 h provided complete dye decomposition, while the final solution still could contain intermediates of aromatic ring cleavage, such as malonic and oxalic acid which absorb in the UV range.

Since the photodegradation of Rd B proceeds through the formation of intermediates, which changes the Rd B absorption, to obtain kinetic curves shown in Fig. 9c, deconvolution using the OMNIC software (Fig. 9a, insets) was carried out. The starting point was aqueous Rd B after its storage in the dark together with catalyst (red spectrum and upper-left inset in Fig. 9a). Its peak can be deconvoluted to two main peaks with their maxima at 520 and 553 nm, corresponding to H-dimers and monomers of Rd B, respectively (metachromasy effect) [75]. Likewise, the spectrum of fully diethylated Rd can be decomposed into two components at 496 and 467 nm (purple curve taken after 7 h and lower-left inset, Fig. 9a). Based on the deconvolution of Rd B and Rd spectra, the transitional spectra were decomposed (see for example, lower-right inset, Fig. 9a), considering that they had components characteristic of both Rd B and Rd in their spectra. The optical density at 520 and 540 nm increased, pointing at the products of incomplete Rd B diethylation, which is why only the peak at 553 nm was used to calculate the Rd B concentration during photocatalytic tests.

Reaction order and rate constants were calculated by means of the differential method in the $|\ln(\Delta C/\Delta t)| - |\ln \Delta C|$ coordinates. The reaction order was calculated from the slope and the ln$K$ was obtained from the intercept (an example is presented in Fig.S6 in *Supplementary Materials*). The obtained kinetic parameters are provided in Table 2.

Table 2
Calculated data on Rd B adsorption and kinetic parameters on its photocatalytic degradation.

Sample	Rd B sorption (%)	K_{app} (min^{-1})	Kinetic order	R^2 (first order curves)
BSO	6	0.0150	0.97	0.975
BSO_hν	10	0.0182	1.00	0.979
P 25	18	0.0424	1.00	0.995

According to the literature, photocatalytic degradation of Rd B dye can be described with the Langmuir kinetic model:

$$r = -\frac{dC}{dt} = \frac{k_r K_{ad} C}{K_{ad} C + 1} \quad (1)$$

where r is the photocatalytic reaction rate, C is the concentration of Rd B at time t (min), k_r the reaction rate constant (min^{-1}), and K_{ad} the adsorption constant of Rd B on catalyst's surface (M^{-1}). The latter adsorption constants were calculated from the adsorption isotherms. Such an isotherm obtained for sample BSO_hν is presented in Fig. 9b. Here, two models were found suitable to fit experimental data, the classic Langmuir (L.) model and the Langmuir-Freundlich (L.-M.) model which is used to describe adsorption on inhomogeneous surfaces (purple and red curves in Fig. 9b, respectively). As the latter model fitted the obtained data better ($R^2 = 0.996$, Fig. 9b), it was chosen to be used for further calculations.

The results of multiplication of Rd B concentration and calculated adsorption constants were found to be low enough ($\sim 10^{-5}$). That is why the $K_{ad}C$ in Eq. (1) could be neglected, leading to the kinetic model of the

first order:

$$\ln\frac{C}{C_0} = -k_r K_{ad} t = -k_{app} t \quad (2)$$

where C_0 is the initial Rd B concentration, C its concentration at time t (min), and k_{app} is the apparent reaction rate constant. The curves plotted in the $\ln C_0/C - t$ coordinated can be linearized (Fig.S7) with R^2 values of 0.975 and 0.979 (for samples BSO_hν and BSO, respectively).

Irradiation of Rd B solution without any catalyst for 8 h was found not to result in any noticeable decomposition, as well seen in Fig. 9c (black triangles). Degradation efficiency achieved in presence of sample BSO was 27 % after 8 h, while sample BSO_hν was able to degrade 100% of Rd B after as long as only 4 h. Sample P 25 was found to cause full decolorization of Rd B after 2 h, while at this point its counterpart sample BSO_hν was able to decay ~ 50% of the dye. Thus, the latter laser-prepared material did not surpass the commercial titania-based standard, but still demonstrated comparable performance even having a lower sorption ability (Table 2).

The catalytic activity of nanomaterials is known often to decrease or even disappear as a result of their interactions with the products of photocatalysis or because of photo-corrosion. That is why stability of sample BSO_hν was tested over repeated photocatalytic cycles, each being run for 8 h. We ran nine identic cycles of Rd B photo-degradation with same BSO_hν material, monitoring Rd B degradation through disappearance of the peak at 495 nm (see curve 8 in Fig. 9a).

It was found that 5×10^{-6} M Rd B could be completely removed from the solution during 4 sequential cycles (Fig. 9d). After cycle 5, some amount of the dye remained in the solution, while after cycle 6, 20% of initial dye still remained untouched. The trend continued, and after cycle 9, almost 50% of Rd B remained intact. Unfortunately, no phase and structural changes of the catalyst could be monitored during this test, as sample BSO_hν has no long-range order and thus cannot be investigated by means of either XRD or Raman methods.

The photocatalytic activity of both catalysts, BSO and BSO_hν, was also studied in the process of pH degradation during 8 h of irradiation. For comparison, a similar experiment with catalyst P 25 as reference was carried out. Phenol is known to be quite a stable model compound with low decomposition rates. Figure S8 shows absorption spectra of pH before and after 8 h of irradiation in presence of sample BSO_hν. It is seen that after 8 h of irradiation in presence of the novel catalyst, the Ph absorption peak decreased, while additional absorption peaks at 240–250 and 380–390 nm appeared. These additional components point at the formation of intermediates, more specifically p-benzoquinone (246 nm) and hydroquinone (389 nm) [76]. Since these components make the determination of remaining phenol concentration difficult, the percentage of decomposition was evaluated from the luminescence spectra of phenol (see Fig.S8, inset). As seen in Fig. 10 and Table 3, only sample BSO_hν catalyzed Ph decomposition, while samples P 25 and BSO were inactive. Thus, while reference catalyst P 25 performed better in case of Rd B, the newly developed sample BSO_hν over-performed it decomposing phenol.

Thus, of all the materials obtained in this work, sample BSO_hν exhibited better photocatalytic performance in decomposing organics, both Rd B and Ph. This can be linked to: (i) the presence of Bi_2SiO_5 in this material; (ii) more homogeneous structure and composition of sample BSO_hν in comparison with its non-irradiated counterpart; (iii) its semiconducting properties which are different from those of sample BSO (lower flat band potential and higher charge carrier mobility). That is, the additional LIC treatment led to formation of an efficient photocatalytically-active material.

4. Conclusion

Two individual colloids of Bi- and Si-based nanoparticles were obtained via laser ablation of corresponding targets in distilled water. The as-prepared colloids were then mixed, after which one part was kept untreated (sample BSO) and the other one was post-treated with the same laser beam (sample BSO_hν). The non-treated sample BSO was found to consist of metallic Bi nanoparticles (as the main component) covered with layers of SiO_2 and amorphous SiO_x, with some products of Bi and Si interaction apparently present at trace amounts. Meanwhile, the post-treated sample BSO_hν clearly demonstrated presence of Bi-Si-O species, implying bismuth silicates as its main component. Thus, exposure of mixed laser-generated Si- and Bi- based colloids to high-power focused pulsed laser radiation is shown to initiate interactions between Bi and Si species, resulting in formation of Bi-O-Si bonds characteristic of bismuth silicates.

More detailed characterization of sample BSO_hν revealed its main product with Bi-Si-O species was metasilicate Bi_2SiO_5 with a band gap of 3.5 eV. Meanwhile, sample BSO exhibited more metallic rather than semiconducting behavior, implying that metallic Bi phase remained mainly unchanged in this material. Both samples were calculated to have high negative values of flat band potential and high donor density. At the same time, the post-irradiated sample exhibited much better charge carrier mobility, implying better potential for photocatalytic applications. Photocatalytic tests carried out with rhodamine B and phenol confirmed that sample BSO_hv indeed decomposed both organics better than its non-irradiated counterpart (sample BSO). Thus, for the first time it was shown that additional post-treatment of mixed individual colloids of Bi and Si nanoparticles led to formation of a photocatalytically-active and stable nanomaterial based on bismuth silicates.

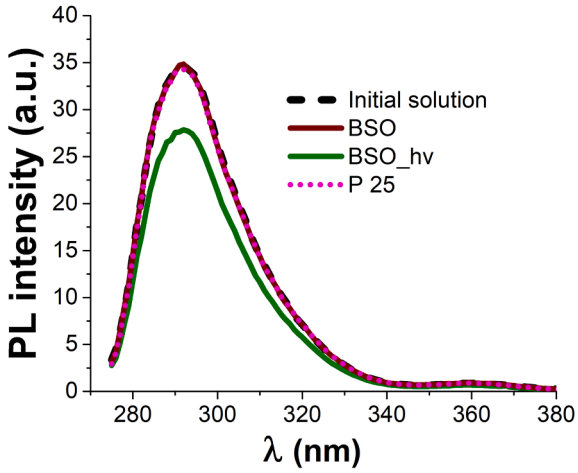

Fig. 10. Photoluminescence spectra of phenol before (black dashed curve) and after photocatalytic test with catalysts: BSO (brown curve), BSO_hv (green curve), P 25 (pink dotted curve). The excitation source used for PL had λ_{ex} = 270 nm. Note that the curves corresponding to initial solution (black), sample BSO (brown) and reference sample P 25 (pink) practically coincide.

Table 3
Phenol decomposition efficiency.

Catalyst	Ph decomposition (%)
None	0
P 25	0
BSO	0
BSO_hν	23

CRediT authorship contribution statement

A.V. Shabalina: Conceptualization, Investigation, Formal analysis, Validation, Methodology, Writing – original draft, Writing – review & editing. **E.D. Fakhrutdinova:** Investigation, Validation, Formal analysis. **A.G. Golubovskaya:** Formal analysis, Investigation, Validation,

Methodology. **S.M. Kuzmin:** Formal analysis, Validation. **S.V. Koscheev:** Methodology, Data curation, Formal analysis, Investigation. **S.A. Kulinich:** Formal analysis, Writing – original draft, Writing – review & editing. **V.A. Svetlichnyi:** Methodology, Project administration, Writing – original draft, Writing – review & editing. **O.V. Vodyankina:** Methodology, Project administration, Writing – review & editing.

Declaration of Competing Interest

The authors declare that they have no known competing financial interests or personal relationships that could have appeared to influence the work reported in this paper.

Acknowledgement

The work was supported by the Russian Science Foundation (project no. 19-73-30026).

Appendix A. Supplementary material

Supplementary data to this article can be found online at https://doi.org/10.1016/j.apsusc.2021.151732.

References

[1] F.R. Akhmedzhanov, S.Z. Mirzaev, U.A. Saidvaliev, Parameters of elastic anisotropy in bismuth silicate crystals, Ferroelectrics 556 (1) (2020) 23–28, https://doi.org/10.1080/00150193.2020.1713335.

[2] S.S. Batool, Z. Imran, K. Rasool, J. Ambreen, S. Hassan, S. Arif, M. Ahmad, M. A. Rafq, Study of electric conduction mechanisms in bismuth silicate nanofbers, Sci. Rep. 10 (2020) 2775, https://doi.org/10.1038/s41598-020-59563-6.

[3] Y. Ke, W. Huang, S.K. Thatikonda, R. Chen, C. Yao, N. Qin, D. Bao, Highly frequency-, temperature-, and bias-stable dielectric properties of 500°C processed Bi_2SiO_5 thin films with low dielectric loss, Curr. Appl. Phys. 20 (2020) 751–754, https://doi.org/10.1016/j.cap.2020.03.010.

[4] K. Sakamoto, M. Hagiwara, H. Taniguchi, S. Fujihara, Fabrication of bismuth silicate Bi_2SiO_5 ceramics as a potential high-temperature dielectric material, J. Mater. Sci. 56 (14) (2021) 8415–8426, https://doi.org/10.1007/s10853-021-05849-7.

[5] M. Back, E. Casagrande, C.A. Brondin, E. Ambrosi, D. Cristofori, J. Ueda, S. Tanabe, E. Trave, P. Riello, Lanthanide-doped Bi_2SiO_5@SiO_2 core−shell upconverting nanoparticles for stable ratiometric optical thermometry, ACS Appl. Nano Mater. 3 (3) (2020) 2594–2604, https://doi.org/10.1021/acsanm.0c00003.

[6] M. Back, E. Casagrande, E. Trave, D. Cristofori, E. Ambrosi, F. Dallo, M. Roman, J. Ueda, J. Xu, S. Tanabe, A. Benedetti, P. Riello, Confined-melting-assisted synthesis of bismuth silicate glass-ceramic nanoparticles: Formation and optical thermometry investigation, ACS Appl. Mater. Interfaces 12 (49) (2020) 55195–55204, https://doi.org/10.1021/acsami.0c17897.

[7] L. Zhang, P. Li, A. Zhao, X. Li, J. Tang, F. Zhang, G. Jia, C. Zhang, Synthesis, structure, and color-tunable luminescence properties of lanthanide activator ions doped bismuth silicate as single-phase white light emitting phosphors, J. Alloy Compd. 816 (2020) 152546, https://doi.org/10.1016/j.jallcom.2019.152546.

[8] L. Zhang, G. Wang, Y. Lu, F. Zhang, G. Jia, C. Zhang, Novel bismuth silicate based upconversion phosphors: Facile synthesis, structure, luminescence properties, and applications, J. Lumin. 216 (2019) 116718, https://doi.org/10.1016/j.jlumin.2019.116718.

[9] H.R. Mahmoud, M. Saif, R. Fouad, Novel multi-functional Pr^{3+}:$Bi_{12}SiO_{20}$ luminescent nano-sensor for latent human prints, iron ions in drinking water and anticounterfeiting application, J. Alloys Compd. 805 (2019) 887–895, https://doi.org/10.1016/j.jallcom.2019.07.097.

[10] J. Bautista-Ruiz, A. Chaparro, W. Bautista, Characterization of bismuth-silicate soles, J. Phys.: Conf. Ser. 1386 (2019) 012020, https://doi.org/10.1088/1742-6596/1386/1/012020.

[11] P.M. Rafailov, V. Marinova, R. Todorov, S. Boyadjiev, An optical excitation study of pure and Ru-doped $Bi_{12}SiO_{20}$ crystals with graphene coating, J. Phys.: Conf. Ser. 1762 (1) (2021) 012024, https://doi.org/10.1088/1742-6596/1762/1/012024.

[12] I.G. Dadenkov, A.L. Tolstik, Y.I. Miksyuk, K.A. Saechnikov, Photoinduced absorption and pulsed recording of dynamic holograms in bismuth silicate crystals, Opt Spectrosc. 128 (9) (2020) 1401–1406, https://doi.org/10.1134/S0030400X20090052.

[13] H.R. Mahmoud, Bismuth silicate ($Bi_4Si_3O_{12}$ and Bi_2SiO_5) prepared by ultrasonic-assisted hydrothermal method as novel catalysts for biodiesel production via oleic acid esterification with methanol, Fuel 256 (2019) 115979, https://doi.org/10.1016/j.fuel.2019.115979.

[14] X. Qin, Y. Huang, Y. Shen, M. Zhao, X. Gao, Porous 3D flower-like bismuth silicate@nitrogen-doped graphene nanomaterial as high-efficient catalyst for fuel cell cathode, Ceram. Int. 45 (18) (2019) 24515–24527, https://doi.org/10.1016/j.ceramint.2019.08.179.

[15] A.V. Zaitsev, E.A. Kirichenko, O.I. Kaminsky, K.S. Makarevich, Investigation into the efficiency of photocatalytic oxidation of aqueous solutions of organic toxins in a unit with an automatically cleaning bismuth-silicate photocatalyst, J. Water Process. Eng. 37 (2020) 101468, https://doi.org/10.1016/j.jwpe.2020.101468.

[16] S.S. Batool, S. Hassan, Z. Imran, K. Rasool, M. Ahmad, M.A. Rafiq, Comparison of different phases of bismuth silicate nanofibers for photodegradation of organic dyes, Int. J. Environ. Sci. Technol. 13 (6) (2016) 1497–1504, https://doi.org/10.1007/s13762-016-0987-2.

[17] K. Karthik, K.R.S. Devi, D. Pinheiro, S. Sugunan, Photocatalytic activity of bismuth silicate heterostructures synthesized via surfactant mediated sol-gel method, Mater. Sci. Semicond. Process. 102 (2019) 104589, https://doi.org/10.1016/j.mssp.2019.104589.

[18] Y. Wu, J. Lu, M. Li, J. Yuan, P. Wu, X. Chang, C. Liu, X. Wang, Bismuth silicate photocatalysts with enhanced light harvesting efficiency by photonic crystal, J. Alloys Compd. 810 (2019) 151839, https://doi.org/10.1016/j.jallcom.2019.151839.

[19] Y. Wu, L. Han, J. Lu, Q. Ning, Preparation of Ag–$Bi_{12}SiO_{20}$/Bi_2SiO_5 with high visible light photocatalytic property: the synergistic effect of the heterojunction and the heterogeneous interface, J. Mater. Sci.: Mater. Electron. 32 (6) (2021) 6976–6983, https://doi.org/10.1007/s10854-021-05404-9.

[20] Y. Wu, X. Chang, M. Li, XiPing Hei, C. Liu, X. Zhang, Studying the preparation of pure $Bi_{12}SiO_{20}$ by Pechini method with high photocatalytic performance, J. Sol-Gel Sci. Technol. 97 (2) (2021) 311–319, https://doi.org/10.1007/s10971-020-05447-0.

[21] K.-L. Jia, J. Qu, S.-M. Hao, F. An, Y.-Q. Jing, Z.-Z. Yu, One-pot synthesis of bismuth silicate heterostructures with tunable morphology and excellent visible light photodegradation performances, J. Colloid Interface Sci. 506 (2017) 255–262, https://doi.org/10.1016/j.jcis.2017.07.040.

[22] W. Cheewasukhanont, P. Limkitjaroenporn, S. Kothan, C. Kedkaew, J. Kaewkhao, The effect of particle size on radiation shielding properties for bismuth borosilicate glass, Radiat. Phys. Chem. 172 (2020) 108791, https://doi.org/10.1016/j.radphyschem.2020.108791.

[23] M L. Krishnan, V. V. Ravi Kanth Kumar, Spectroscopic investigations of $AgNO_3$ doped bismuth silicate glasses. AIP Conf. Proc. 2265 (2020) 030223. doi:10.1063/5.0017514.

[24] A. Veber, M.R. Cicconi, A. Puri, D. de Ligny, Optical properties and bismuth redox in Bi-doped high-silica Al−Si Glasses, J. Phys. Chem. C 122 (34) (2018) 19777–19792, https://doi.org/10.1021/acs.jpcc.8b05614.

[25] L. Zhang, P. Li, S. Lv, Y. Lu, X. Li, C. Zhang, G. Jia, Facile synthesis, structure, and tunable luminescence properties of novel one-dimensional $Bi_4Si_3O_{12}$ fibers, CrystEngComm 22 (11) (2020) 2002–2012, https://doi.org/10.1039/C9CE01959F.

[26] Z.H. Bai, X.W. Ba, R. Jia, B. Liu, Z. Xiao, X. Zhang, Preparation and characterization of bismuth silicate nanopowders, Front. Chem. China 2 (2) (2007) 131–134, https://doi.org/10.1007/s11458-007-0027-3.

[27] J. Lu, X. Wang, Y. Wu, Y. Xu, Synthesis of Bi_2SiO_5 powder by molten salt method, Mater. Lett. 74 (2012) 200–202, https://doi.org/10.1016/j.matlet.2012.01.111.

[28] H.D. Xie, C. Jia, Y. Jiang, X.C. Wang, Synthesis of $Bi_4Si_3O_{12}$ powders by a sol–gel method, Mater. Chem. Phys. 133 (2–3) (2012) 1003–1005, https://doi.org/10.1016/j.matchemphys.2012.02.005.

[29] M. Back, E. Trave, G. Zaccariello, D. Cristofori, P. Canton, A. Benedetti, P. Riello, P, Riello, Bi_2SiO_5@g-SiO_2 upconverting nanoparticles: a bismuth-driven core–shell self-assembly mechanism, Nanoscale 11 (2) (2019) 675–687, https://doi.org/10.1039/C8NR08649D.

[30] L. Zhang, W.Z. Wang, S. Sun, J. Xu, M. Shang, J. Ren, Hybrid Bi_2SiO_5 mesoporous microspheres with light response for environment decontamination, Appl. Catal. B 100 (1–2) (2010) 97–101, https://doi.org/10.1016/j.apcatb.2010.07.018.

[31] D. Sarkar, K.S. Paliwal, S. Ganguli, A.E. Praveen, D. Saha, V. Mahalingam, Engineering of oxygen vacancy as defect sites in silicates for removal of diverse organic pollutants and enhanced aromatic alcohol oxidation, J. Environ. Chem. Eng. 9 (2) (2021) 105134, https://doi.org/10.1016/j.jece:2021.105134.

[32] R.N. Yastrebinskii, G.G. Bondarenko, A.V. Pavlenko, Synthesis of stable bismuth silicate with sillenite structure in the Na_2O–Bi_2O_3–SiO_2 system. Inorg. Mater. Appl. Res. 9 (2018) 221-226. doi:10.1134/S2075113318020326.

[33] H.B. Zeng, X.W. Du, S.C. Singh, S.A. Kulinich, S. Yang, J.P. He, W. Cai, Nanomaterials via laser ablation/irradiation in liquid: A review, Adv. Funct. Mater. 22 (7) (2012) 1333–1353, https://doi.org/10.1002/adfm.201102295.

[34] N. Tarasenka, E. Shustava, A. Butsen, A.A. Kuchmizhak, S. Pashayan, S.A. Kulinich, N. Tarasenko, Laser-assisted fabrication and modification of copper and zinc oxide nanostructures in liquids for photovoltaic applications, Appl. Surf. Sci. 554 (2021) 149570, https://doi.org/10.1016/j.apsusc.2021.149570.

[35] R.C. Forsythe, C.P. Cox, M.K. Wilsey, A.M. Müller, Pulsed Laser in Liquids Made Nanomaterials for Catalysis, Chem. Rev. 121 (13) (2021) 7568–7637, https://doi.org/10.1021/acs.chemrev.0c01069.

[36] J.Q. Wang, C. Xi, M. Wang, L. Shang, J. Mao, C.K. Dong, H. Liu, S.A. Kulinich, X. W. Du, Laser-generated grain boundaries in ruthenium nanoparticles for boosting oxygen evolution reaction, ACS Catal. 10 (21) (2020) 12575–12581, https://doi.org/10.1021/acscatal.0c03406.

[37] V. Amendola, D. Amans, Y. Ishikawa, N. Koshizaki, S. Scirè, G. Compagnini, S. Reichenberger, S. Barcikowski, Room-temperature laser synthesis in liquid of oxide, metal-oxide core-shells, and doped oxide nanoparticles, Chem. Eur. J. 26 (42) (2020) 9206–9242, https://doi.org/10.1002/chem.202000686.

[38] S.O. Gurbatov, E. Modin, V. Puzikov, P. Tonkaev, D. Storozhenko, A. Sergeev, N. Mintcheva, S. Yamaguchi, N.N. Tarasenka, A. Chuvilin, S. Makarov, S. A. Kulinich, A.A. Kuchmizhak, Black Au-decorated TiO_2 produced via laser

ablation in liquid, ACS Appl. Mater. Interfaces 13 (5) (2021) 6522–6531, https://doi.org/10.1021/acsami.0c20463.
[39] G. Lin, D. Tan, F.F. Luo, D. Chen, Q.Z. Zhao, J. Qiu, Z. Xu, Fabrication and photocatalytic property of α-Bi_2O_3 nanoparticles by femtosecond laser ablation in liquid, J. Alloys. Compd. 507 (2) (2010) L43–L46, https://doi.org/10.1016/j.jallcom.2010.08.014.
[40] S. Dadashi, R. Poursalehi, H. Delavari, Optical and structural properties of Bi-based nanoparticles prepared via pulsed Nd:YAG laser ablation in organic liquids, Appl. Phys. A 124 (2018) 406–413, https://doi.org/10.1007/s00339-018-1817-9.
[41] V.A. Svetlichnyi, Y.A. Belik, A.A. Vodyankin, E.D. Fakhrutdinova, O. V. Vodyankina, Laser fragmentation of photocatalyst particles based on bismuth silicates, Proc. SPIE 11322 (2019) 113221D, https://doi.org/10.1117/12.2550779.
[42] V.A. Svetlichnyi, A.V. Shabalina, I.N. Lapin, D.A. Goncharova, T.S. Kharlamova, A. I. Stadnichenko, Comparative study of magnetite nanoparticles obtained by pulsed laser ablation in water and air, Appl. Surf. Sci. 467-468 (2019) 402–410, https://doi.org/10.1016/j.apsusc.2018.10.189.
[43] A.V. Shabalina, T.I. Izaak, T.S. Kharlamova, D.O. Martynova, I.N. Lapin, V. A. Svetlichnyi, Ag/SiO_x nanocomposite powders synthesized from colloids obtained by pulsed laser ablation, Colloids Surf. A 553 (2018) 80–88, https://doi.org/10.1016/j.colsurfa.2018.05.047.
[44] V.A. Svetlichnyi, T.I. Izaak, I.N. Lapin, D.O. Martynova, O.A. Stonkus, A. I. Stadnichenko, A.I. Boronin, Physicochemical investigation of nanopowders prepared by laser ablation of crystalline silicon in water, Adv. Powder Technol. 26 (2) (2015) 478–486, https://doi.org/10.1016/j.apt.2014.12.004.
[45] V.A. Svetlichnyi, E.D. Fakhrutdinova, T.S. Nazarova, S.A. Kulinich, O. V. Vodyankina, Comparative study of bismuth composites obtained via pulsed laser ablation in a liquid and in air for photocatalytic application, Solid State Phenom. 312 (2020) 172–178, https://doi.org/10.4028/www.scientific.net/SSP.312.172.
[46] J.C. Bulmahn, G. Tikhonowski, A.A. Popov, A. Kuzmin, S.M. Klimentov, A. V. Kabashin, P.N. Prasad, Laser-ablative synthesis of stable aqueous solutions of elemental bismuth anoparticles for multimodal theranostic applications, Nanomaterials 10 (2020) 1463, https://doi.org/10.3390/nano10081463.
[47] N. Haustrup, G.M. O'Connor, Nanoparticle generation during laser ablation and laser-induced liquefaction, Physics Procedia 12 (2011) 46–53, https://doi.org/10.1016/j.phpro.2011.03.104.
[48] C.Y. Shih, M.V. Shugaev, C.P. Wu, L.V. Zhigilei, The effect of pulse duration on nanoparticle generation in pulsed laser ablation in liquids: insights from large-scale atomistic simulations, Phys. Chem. Chem. Phys. 22 (13) (2020) 7077–7099, https://doi.org/10.1039/D0CP00608D.
[49] D.A. Zatsepin, A.F. Zatsepin, D.W. Boukhvalov, N.V. Gavrilov, Bi-doped silica glass: A combined XPS – DFT study of electronic structure and pleomorphic imperfections, J. Alloys Compd. 829 (2020) 154459, https://doi.org/10.1016/j.jallcom.2020.154459.
[50] Y.J. Shu, S.R. Yan, K.J. Dong, J.W. Chen, Preparation of Novel Mesoporous Photocatalyst Bi_4O_5Br 2/SBA-15 with Enhanced Visible-Light Catalytic Activity, J. Appl. Sci. 8 (2018) 532–544, https://doi.org/10.4236/ojapps.2018.811043.
[51] R. Köhler, D. Siebert, L. Kochanneck, G. Ohms, W. Viöl, Bismuth oxide faceted structures as a photocatalyst produced using an atmospheric pressure plasma Jet, Catalysts 9 (2019) 533, https://doi.org/10.3390/catal9060533.
[52] V.S. Dharmadhikari, S.R. Sainkar, S. Badrinarayan, A. Goswami, Characterisation of thin films of bismuth oxide by X-ray photoelectron spectroscopy, J. Electron Spectrosc. Relat. Phenom. 25 (2) (1982) 181–189, https://doi.org/10.1016/0368-2048(82)85016-0.
[53] G. Wittstock, A. Strübing, R. Szargan, G. Werner, Glucose oxidation at bismuth-modified platinum electrodes, J. Electroanal. Chem. 444 (1) (1998) 61–73, https://doi.org/10.1016/S0022-0728(97)00559-7.
[54] L. Dou, X. Jin, J. Chen, J. Zhong, J.Z. Li, Y. Zeng, R. Duan, One-pot solvothermal fabrication of S-scheme OVs-Bi_2O_3/Bi_2SiO_5 microsphere heterojunctions with enhanced photocatalytic performance toward decontamination of organic pollutants, Appl. Surf. Sci. 527 (2020) 146775, https://doi.org/10.1016/j.apsusc.2020.146775.
[55] Y. Belik, T. Kharlamova, A. Vodyankin, V. Svetlichnyi, O. Vodyankina, Mechanical activation for soft synthesis of bismuth silicates, Ceram. Int. 46 (8) (2020) 10797–10806, https://doi.org/10.1016/j.ceramint.2020.01.090.
[56] L. Li, Y. Long, Y. Chen, S. Wang, L. Wang, S. Zhang, F. Jiang, Facile synthesis of Fe/Bi_2SiO_5 nanocomposite with enhanced photocatalytic activity for degradation of 17β-Estradiol(E2), Solid State Sci. 83 (2018) 143–151, https://doi.org/10.1016/j.solidstatesciences.2018.07.008.
[57] M.H. Brodsky, M. Cardona, J.J. Cuomo, Infrared and Raman spectra of the silicon–hydrogen bonds in amorphous silicon prepared by glow discharge and sputtering. Phys. Rev. B 16 (1977) 3556-3571. doi:10.1103/physrevb.16.3556.
[58] V. Drinek, Z. Bastl, J. Subrt, A. Yabe, J. Pola, IR laser-induced reactive ablation of silicon monoxide in hydrogen and water atmosphere, J. Mater. Chem. 12 (2002) 1800–1805, https://doi.org/10.1039/b200058j.
[59] D. Liu, W. Yao, J. Wang, Y. Liu, M. Zhang, Y. Zhu, Enhanced visible light photocatalytic performance of a novel heterostructured $Bi_4O_5Br_2$/$Bi_{24}O_{31}Br_{10}$/Bi_2SiO_5 photocatalyst, Appl. Catal. B 172–173 (2015) 100–107, https://doi.org/10.1016/j.apcatb.2015.01.037.
[60] J.H. Parker Jr., D.W. Feldman, M. Ashkin, Raman scattering by silicon and germanium, Phys. Rev. 155 (1967) 712–714, https://doi.org/10.1103/physrev.155.712.
[61] N. Hussain, T.X. Liang, Q. Zhang, T. Anwar, Y. Huang, J.L. Lang, K. Huang, H. Wu, Ultrathin Bi nanosheets with superior photoluminescence, Small 13 (36) (2017) 1701349, https://doi.org/10.1002/smll.201701349.
[62] J.A. Steele, R.A. Lewis, In situ micro-Raman studies of laser-induced bismuth oxidation reveals metastability of β-Bi_2O_3 microislands, Opt. Mater. Express 4 (2014) 2133–2142, https://doi.org/10.1364/ome.4.002133.
[63] K. Trentelman, A note on the characterization of bismuth black by Raman microspectroscopy, J. Raman Spectrosc. 40 (5) (2009) 585–589, https://doi.org/10.1002/jrs.v40:510.1002/jrs.2184.
[64] B. Chai, J. Yan, G. Fan, G. Song, C. Wang, In-situ construction of Bi_2SiO_5/BiOBr heterojunction with significantly improved photocatalytic activity under visible light, J. Alloy. Compd. 802 (2019) 301–309, https://doi.org/10.1016/j.jallcom.2019.06.195.
[65] F.D. Hardcastle, I.E. Wachs, The molecular structure of bismuth oxide by Raman spectroscopy, J. Solid State Chem. 97 (2) (1992) 319–331, https://doi.org/10.1016/0022-4596(92)90040-3.
[66] Y. Wu, M. Li, J. Yuan, X. Wan, Synthesis and characterizations of metastable Bi_2SiO_5 powders with a synergistic effect of adsorption and photocatalysis, Appl. Phys. A 123 (2017) 543, https://doi.org/10.1007/s00339-017-1144-6.
[67] C. Ayik, I. Studenyak, M. Kranjec, M. Kurik, Urbach rule in solid state physics, Int. J. Opt. Appl. 4 (3) (2014) 76–83, https://doi.org/10.5923/j.optics.20140403.02.
[68] S.J. Ikhmayies, R.N. Ahmad-Bitar, A study of the optical bandgap energy and Urbach tail of spray-deposited CdS: In thin films, J. Mater. Res. Technol. 2 (3) (2013) 221–227, https://doi.org/10.1016/j.jmrt.2013.02.012.
[69] A. Amato, S. Terreni, M. Granata, C. Michel, B. Sassolas, L. Pinard, M. Canepa, G. Cagnoli, Observation of a correlation between internal friction and Urbach energy in amorphous oxides thin films, Sci. Rep. 10 (2020) 1670, https://doi.org/10.1038/s41598-020-58380-1.
[70] A. Hankin, F.E. Bedoya-Lora, J.C. Alexander, A. Regoutz, G.H. Kelsall, Flat band potential determination: avoiding the pitfalls, J. Mater. Chem. A 7 (45) (2019) 26162–26176, https://doi.org/10.1039/C9TA09569A.
[71] D. Clymer, M. Matin, Application of Mott-Gurney law to model the current voltage relationship of PPV/CN-PPV with a thin-metal anode buffer, Proc. SPIE 5907 (2005) 59070S, https://doi.org/10.1117/12.612651.
[72] Z.B. Wang, M.G. Helander, M.T. Greiner, J. Qiu, Z.H. Lu, Carrier mobility of organic semiconductors based on current-voltage characteristics. J. Appl. Phys. 107 (2010) 034506. doi:10.1063/1.3305341.
[73] A.A. Isari, A. Payan, M. Fattahi, S. Jorfi, B. Kakavandi, Photocatalytic degradation of rhodamine B and real textile wastewater using Fe-doped TiO_2 anchored on reduced graphene oxide (Fe-TiO_2/rGO): Characterization and feasibility, mechanism and pathway studies, Appl. Surf. Sci. 462 (2018) 549–564, https://doi.org/10.1016/j.apsusc.2018.08.133.
[74] X.F. Hu, T. Mohamood, W.H. Ma, C.C. Chen, J.C. Zhao, Oxidative decomposition of rhodamine B dye in the presence of VO_2^+ and/or Pt(IV) under visible light irradiation: N-deethylation, chromophore cleavage, and mineralization, J. Phys. Chem. B 110 (2006) 26012–26018, https://doi.org/10.1021/jp063588q.
[75] Z. Grauer, A.B. Malter, S. Yariv, D. Avnir, Sorption of rhodamine B by montmorillonite and laponite, Colloid. Surf. 25 (1) (1987) 41–65, https://doi.org/10.1016/0166-6622(87)80268-8.
[76] X.Q. Wang, F. Wang, B. Chen, K. Cheng, J.L. Wang, J.J. Zhang, H. Song, Promotion of phenol photodecomposition and the corresponding decomposition mechanism over g-C_3N_4/TiO_2 nanocomposites, Appl. Surf. Sci. 453 (2018) 320–329, https://doi.org/10.1016/j.apsusc.2018.05.082.